

Label-Free Intracellular Multi-Specificity in Yeast Cells by Phase-Contrast Tomographic Flow Cytometry

Vittorio Bianco,* Massimo D'Agostino, Daniele Pirone, Giusy Giugliano, Nicola Mosca, Maria Di Summa, Gianluca Scerra, Pasquale Memmolo, Lisa Miccio,* Tommaso Russo, Ettore Stella, and Pietro Ferraro

In-flow phase-contrast tomography provides a 3D refractive index of label-free cells in cytometry systems. Its major limitation, as with any quantitative phase imaging approach, is the lack of specificity compared to fluorescence microscopy, thus restraining its huge potentialities in single-cell analysis and diagnostics. Remarkable results in introducing specificity are obtained through artificial intelligence (AI), but only for adherent cells. However, accessing the 3D fluorescence ground truth and obtaining accurate voxel-level co-registration of image pairs for AI training is not viable for high-throughput cytometry. The recent statistical inference approach is a significant step forward for label-free specificity but remains limited to cells' nuclei. Here, a generalized computational strategy based on a self-consistent statistical inference to achieve intracellular multi-specificity is shown. Various subcellular compartments (i.e., nuclei, cytoplasmic vacuoles, the peri-vacuolar membrane area, cytoplasm, vacuole-nucleus contact site) can be identified and characterized quantitatively at different phases of the cells life cycle by using yeast cells as a biological model. Moreover, for the first time, virtual reality is introduced for handling the information content of multi-specificity in single cells. Full fruition is proofed for exploring and interacting with 3D quantitative biophysical parameters of the identified compartments on demand, thus opening the route to a metaverse for 3D microscopy.

1. Introduction

Fluorescence imaging flow cytometry (FIFC) is the current gold standard for high-throughput single-cell analysis, diagnostics, and cell biology studies. FIFC can analyze heterogeneous cell populations with statistical relevance while describing their intraspecies variability.^[1] FIFC relies on fluorescent markers that bind to targeted molecules or functional groups of them to localize subcellular organelles. Such intracellular multi-specificity is a powerful probing tool to gather information on the cells' structure, inner regulatory mechanisms, life cycle, drug reaction, and external cues.^[1-3] However, using markers, dyes or stains is emerging as a severe limitation for the non-invasive observation of cells. Fluorescent assays are sample preparation-dependent, expensive, time-consuming, and require prior knowledge of the exogenous contrast agents. Above all, cell labeling can lead to photobleaching and phototoxicity.^[3] In addition, in


FIFC the single-cell analysis is only qualitative, while unfortunately cells' biophysical properties cannot be measured from the recorded images. Quantitative phase imaging (QPI) is a label-free and quantitative alternative to fluorescence microscopy (FM).^[4-6] They aim to recover the quantitative phase-contrast map (QPM) of the sample from one or more images captured by a light-intensity sensor. In this framework, digital holography (DH)^[7,8] is one of the preferable solutions for microfluidic environments thanks to its capability to image flowing samples out-of-focus in the form of a modulated fringe pattern and to refocus them in post-processing.^[9] In a QPM, the cell's inner contrast is endogenous, and due to the phase delay introduced by the specimen on the light probe, no dye is employed. However, in a 2D QPM, the 3D cell's morphology is coupled to the 3D cell's refractive index (RI). Phase contrast tomography (PCT) retrieves the 3D volumetric distribution of the cell's RIs and its biophysical features (e.g., dry mass) by combining several QPMs captured at different viewing angles.^[10,11] Two recording approaches are usually adopted in PCT. In the former, cells are fixed at rest on a surface and are recorded along several viewing directions by means of an illumination scanning (IS) method.^[5] This method excludes

V. Bianco, D. Pirone, G. Giugliano, P. Memmolo, L. Miccio, P. Ferraro
CNR-ISASI

Institute of Applied Sciences and Intelligent Systems "E. Caianiello"
Via Campi Flegrei 34, Pozzuoli, Napoli 80078, Italy
E-mail: v.bianco@isasi.cnr.it; lisa.miccio@isasi.cnr.it

M. D'Agostino, G. Scerra, T. Russo
Department of Molecular Medicine and Medical Biotechnology
University of Naples "Federico II"
Via S. Pansini 5, Naples 80131, Italy

N. Mosca, M. Di Summa, E. Stella
Institute of Intelligent Industrial Technologies and Systems for Advanced
Manufacturing
National Research Council of Italy
Via Amendola 122/D-O, Bari 70125, Italy

 The ORCID identification number(s) for the author(s) of this article can be found under <https://doi.org/10.1002/smt.202300447>

© 2023 The Authors. Small Methods published by Wiley-VCH GmbH.
This is an open access article under the terms of the Creative Commons Attribution-NonCommercial License, which permits use, distribution and reproduction in any medium, provided the original work is properly cited and is not used for commercial purposes.

DOI: 10.1002/smt.202300447

the possibility to analyze samples that naturally live in suspension (e.g., blood cells), and cannot be applied in FC conditions. In the latter, cells are suspended and rotated by means of optical or acoustic forces while they are illuminated along a fixed beam direction.^[12,13] Conversely, in-flow PCT^[14] reconstructs 3D RI tomograms of suspended cells in high-throughput microfluidic streams.^[15] In-flow PCT exploits a controlled rotation of the samples while they travel along the microfluidic channels to probe them from different directions. Thus, PCT can work in FC modality (hereafter named PCT-FC) without mechanical/optical changes to the recording system.^[14–17]

However, the advantages of PCT and PCT-FC are counterbalanced by the lack of intracellular specificity. Since no dye is employed, it is not trivial to recognize and isolate a certain organelle inside the cell from the dense distribution of RI values of the 3D tomogram. Only in a few cases, RI thresholding identify structures from high-contrast tomograms of cells spread out on a surface.^[18–23] Virtual staining constitutes the first attempt to bridge the intracellular specificity gap between fluorescence microscopy and label-free microscopy. It has been demonstrated for 2D QPMs of label-free tissues^[24–26] and cells.^[27,28] Then, it was extended to the 3D case at the single-cell level.^[29] Remarkably, several organelles (actin, plasma membrane, mitochondria, nucleus, nucleoli) have been virtually stained in the same cell.^[30] Virtual staining is based on training a deep learning model by pairs of co-registered 3D examples made of the label-free RI tomograms and the corresponding fluorescence tomograms with the searched organelles appropriately marked. However, creating a 3D dataset with a voxel-level mapping between the RI values and the fluorescence information is not viable in PCT-FC due to the recording of cells in the flow modality. So far, 3D virtual staining has been demonstrated only in the case of a PCT-IS configuration, thus lacking the high-throughput condition requested by statistically significant biological studies. We have recently demonstrated that the specificity gap can be filled in PCT-FC while avoiding deep learning. In particular, we have proposed the Computational Segmentation based on the statistical inference (CSSI) strategy to segment the nucleus inside cancer cells.^[31] This statistical approach avoids the examples provided by a fluorescence channel. Instead, the CSSI method recognizes the statistical similarities among groups of RI voxels within the tomogram to cluster them as belonging or not to the searched volume. The CSSI method works accurately in segmenting the cell nucleus, starting from the hypothesis that it passes for the center of the cell. Generalizing the algorithm to isolate other cellular components/organelles with different RI distributions has never been attempted so far. Another important open issue to be addressed is benchmarking the CSSI performance in the presence of lower-quality tomograms. Since CSSI is based on statistical tests on groups of voxels, its accuracy is in principle limited when organelles too small with respect to the imaging spatial resolution have to be isolated.^[31] Here we demonstrate that the CSSI algorithm can be effectively extended to furnish multiple-specificity at the subcellular level in 3D tomograms of flowing label-free cells. CSSI is applied to lower-resolution tomograms reconstructed using the less-demanding and much faster filtered back projection (FBP) method.^[10] We prove the automatic and simultaneous identification of different intracellular sub-compartments such as nuclei, cytoplasmic vacuoles, the peri-vacuolar membrane re-

gion, cytoplasm, nucleus-vacuoles contact areas, from 3D RI tomograms of yeast cells in different phases/stages of their life cycle. With the aim to develop, optimize, and test such a system, a 3D biological model naturally exhibiting vacuoles was needed. We selected yeast cells as a tunable biological model to test the CSSI capability to isolate cytoplasmic vacuoles from 3D RI tomograms. Identifying vacuoles in budding yeast cells is challenging since the vacuolar size after reshaping is much lower than the resolution limit calculated for the CSSI algorithm.^[31] For this reason, here we propose a strategy to go beyond this limit and segment smaller organelles.

We demonstrate the segmentation of several sub-compartments in flowing yeast cells at different phases, hereafter also indicated as “stages”, of the budding process. Indeed, we show that applying CSSI for segmenting the vacuole allows the downstream identification of the volume containing the vacuolar membrane (whose morphology, integrity, and composition are particularly relevant for the overall activity of the vacuolar compartment,^[32] including the cellular homeostasis, metabolism, and lifespan^[33,34]), the further segmentation of the nucleus, the identification of the nucleus-vacuoles contact volume, and the cytoplasm. The results shown in this work are another critical step toward the highly sought intracellular multi-specificity in the framework of the PCT-FC technology.

2. Results

The PCT-FC system and the numerical processing described in the Experimental section have been employed to reconstruct the 3D RI tomograms of flowing yeast cells. In the PCT-FC paradigm, multiple digital holograms per cell are recorded while it flows and rotates along a microfluidic channel. By keeping the illumination direction fixed, the same cell is thus probed from several viewing angles. From all the digital holograms of a single cell, the corresponding QPMs are numerically extracted and, after estimating the corresponding set of viewing angles, ϑ (angle tracking), the RI volumetric distribution at the single-cell level is obtained. An example of QPM of a yeast cell is displayed in **Figure 1a**. The corresponding 3D RI tomogram, $T = T\{\{\vartheta, QPM\}\}$, is shown in **Figure 1b** via isolevel representation of its 3D external shape and in **Figure 1c** by means of its central slice. The cell cycle of a budding yeast cell (**Figure S1a**, Supporting Information) generally comprises G1, S, G2, and M phases, but the latter largely overlap inside yeast cells.^[35] During the G1 phase, the cell prepares to split. Hence, at the end of the G1 phase, a myosin ring appears where the bud will emerge during the S phase. Moreover, during the S phase, a copy of the genetic material is synthesized, therefore, during the last G2/M phase, the genetic material (e.g., the nucleus) moves inside the bud, thus creating the daughter cell that will be finally detached at the end of the division process.^[35]

In the reported experiments, flowing yeast cells at different stages have been observed. In particular, the yeast cell in **Figure 1a–c** has been caught at the early G1 phase (see **Movie S1**, Supporting Information). In **Figure 1d–f** we report the QPM and the PCT-FC reconstruction of a yeast cell at the late G1 phase (see also **Movie S2**, Supporting Information), where we observe a small bud starting to emerge on the right side (see the arrow in the figure). Furthermore, a yeast cell at the S phase with a more prominent bud is shown in **Figure 1g–i** (see **Movie S3**,

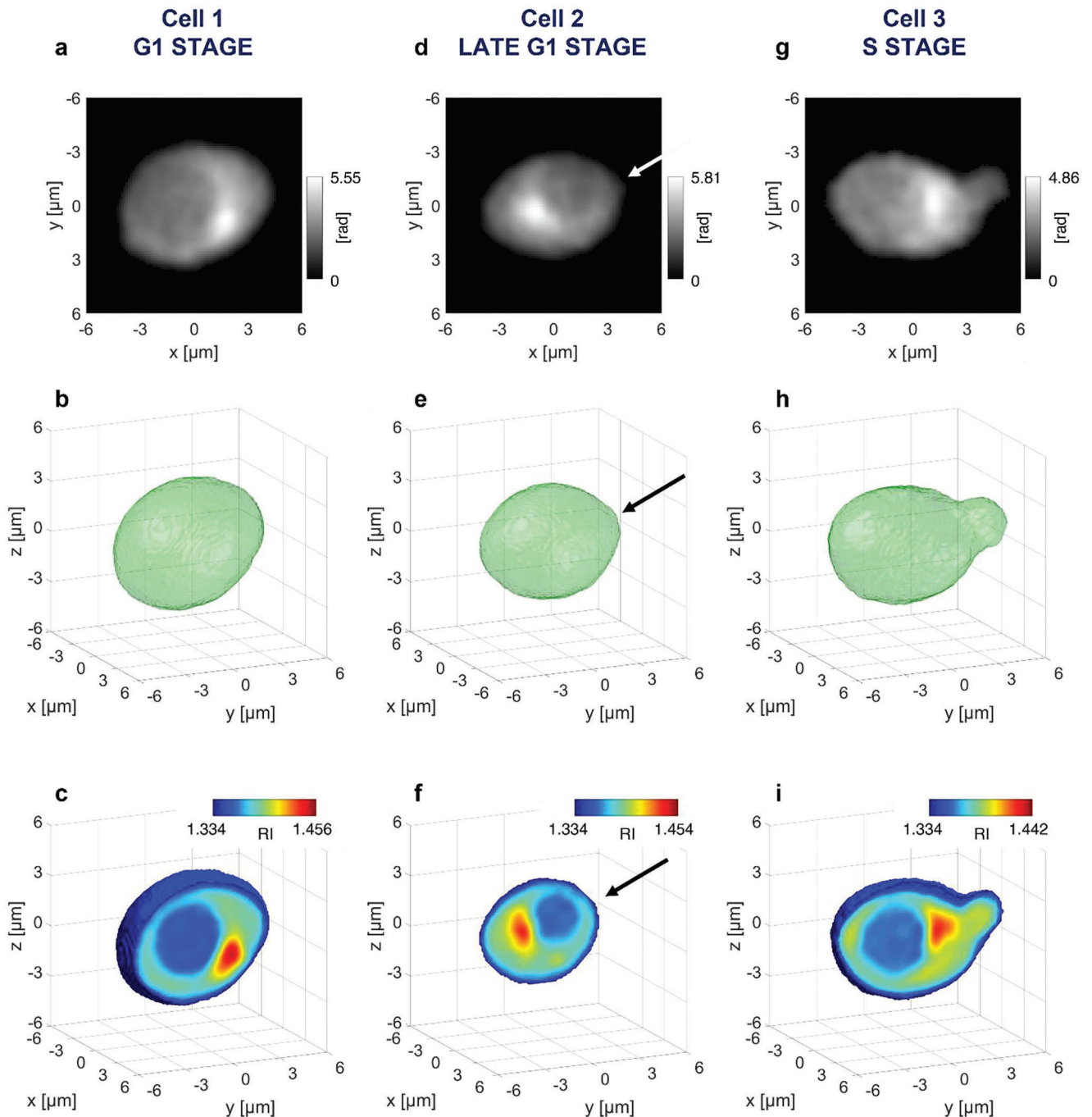


Figure 1. PCT-FC of budding yeast cells at the a–c) G1 stage, d–f) late G1 stage, and g–i) S stage (see also Movies S1–S3, Supporting Information). a, d, g) Example of QPM taken from the overall sequence used to reconstruct the 3D RI tomogram. b, e, h) 3D external shape of the yeast cell after tomographic reconstruction. c, f, i) Central slice of the 3D RI tomogram. In (d–f), the arrows indicate the small emerging bud. In (g–i), the prominent bud is visible on the right.

Supporting Information). The final G2/M case will be discussed later. Referring to Figure 1e, f, it is worth underlining that the ability of PCT-FC to record suspended cells instead of adherent cells is fundamental to reproducing very small changes in the 3D shape of a yeast cell due to the very early budding process. In addition to the sole 3D shape retrieval, PCT-FC allows observing the RI distribution inside the cell during the different phases of

the budding process. The RI values depend on the biophysical features (mechanical, electrical, and optical) of the biological sample and its biochemical composition.^[11] As the vacuoles mainly have an aqueous content, they are clearly visible in the 3D RI tomograms in Figure 1c, f, i in correspondence with the lower values (see the inner blue regions). Consequently, they can be segmented in each cell by setting a suitable RI

threshold. However, as also suggested by the different color bars in Figure 1c,f,i, due to the intra-species variability in the distribution of the sub-compartments, cellular populations are so heterogeneous that the same RI threshold cannot be optimal for all the cells of a certain population. Hence, in a PCT-FC experiment in which hundreds/thousands of cells are recorded, thresholding is not reliable enough.

2.1. Generalized CSSI

The recently developed CSSI accurately isolates the 3D nuclear volume inside the RI tomograms of suspended cells reconstructed by PCT-FC.^[31] CSSI is based on the property that different organelles inside the cell have different statistical distributions of their RI values.^[11] So far, it has been demonstrated to work only for the segmentation of the nucleus inside human cancer cells. For this purpose, the central voxels of the tomogram have been chosen as reference set since, in most cancer cell lines, it is reasonable to assume that the nucleus passes for the center of the cell. As it is based on a statistical working principle, in theory, the CSSI strategy is expected to work for segmenting any organelle inside the cell by changing every time reference set and by slightly adapting the algorithm to the specific cases. However, we have also demonstrated an intrinsic limitation of this statistical approach,^[31] that is related to the statistical power of a hypothesis test. In fact, the CSSI algorithm fails in segmenting organelles that are too small with respect to the imaging spatial resolution of the PCT-FC system, since the lower the number of voxels covered by a certain organelle, the lower the statistical power of the hypothesis test, and then the lower the accuracy of the statistical segmentation. In particular, by means of a 3D numerical cell phantom, we have proved that an organelle with an equivalent radius lower than 15 pixels cannot be identified by CSSI. To counteract this limitation, the state-of-the-art learning tomography (LT) algorithm has been exploited to enhance the intracellular resolution in the tomographic reconstruction.^[31] However, LT-based reconstructions take tens of minutes per cell, which is a too-long computational time for high-throughput experiments. Instead, here we consider a worse case in terms of imaging spatial resolution since we reconstruct the tomograms through the faster but less-performing FBP algorithm. In this way, we significantly save computational time, since the tomographic reconstruction takes only a few seconds per cell. Therefore, the theoretical lower bound of 15 pixels is expected to further increase in this case study. In addition, yeast cells measure about half of human cancer cells, therefore the size of the inner vacuole results in being smaller than the CSSI lower bound established in our previous work.^[31] In general, the assumption of knowing a starting voxel belonging to the organelle to be segmented statistically could be another important limiting factor for generalizing CSSI to subcellular structures other than the nucleus. For the above-mentioned reasons, the original CSSI algorithm would fail in segmenting the vacuoles in these experimental test cases.

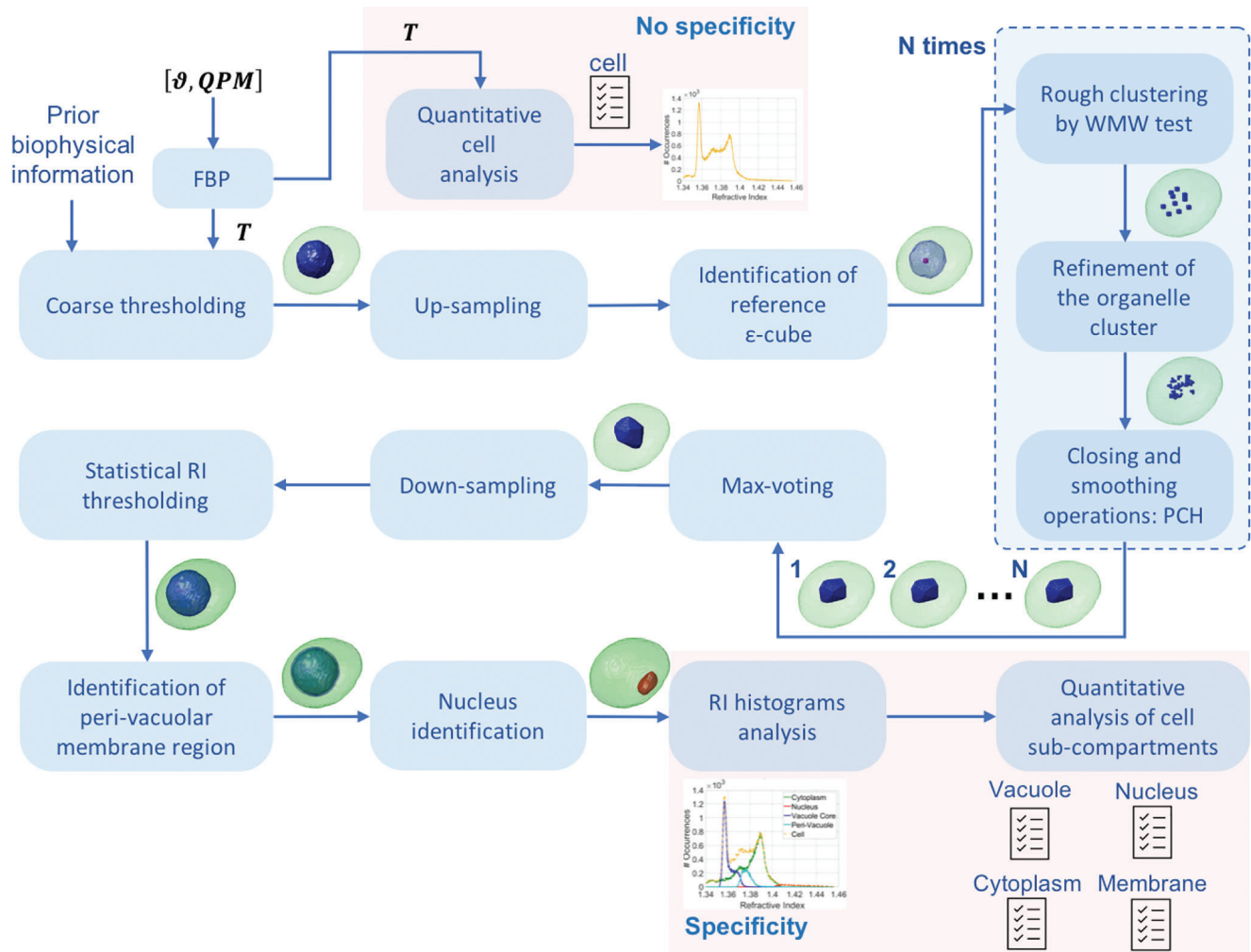
Here we report the generalization of the CSSI method to cope with these cases and to extend it to other organelles and cell sub-compartments. This strategy allows for overcoming the limitation related to the imaging spatial resolution and considering organelles having RI statistical distributions and intracellular lo-

cations completely different from the nucleus ones. In order to show the CSSI steps for the vacuole segmentation, we considered the yeast cell at the G1 phase reported in Figure 1a–c.

Summarizing, we introduced two main differences with respect to the original CSSI. The former is the use of prior biophysical information to identify a reference ϵ -cube (after rough segmentation based on a prior information-guided threshold). Here we can consider intracellular compartments that don't occupy necessarily the central voxel. A further new improvement involves the use of an upsampling-downsampling scheme. Indeed, the ϵ value that determines the size of the voxel cubes cannot go under 8 pixels in order to ensure enough statistical power for the hypothesis test. In principle, organelles having an equivalent radius lower than 15 pixels cannot be segmented since they are covered by very few distinct cubes with edges measuring 8 pixels. The yeast cells considered in this work are very small with respect to the imaging spatial resolution of our optical recording system, thus their size is close to the lower bound of 15 pixels needed to implement the CSSI algorithm. For this reason, up-sampling followed by down-sampling numerically overcomes the issue related to a too-low statistical resolution. This additional strategy makes the CSSI capable of converging to smaller segmented volumes.

The main steps of the generalized CSSI (see also Movie S1, Supporting Information) are sketched in **Scheme 1**, and hereafter detailed.

- Coarse thresholding in Scheme 1 – To choose a reference set, a first rough intra-vacuolar volume (see the blue volume in the isolevels representation of Figure S2a, Supporting Information) is obtained by considering the cellular voxels having RI values lower than a fixed RI threshold. Prior biophysical information is employed at this step to establish the threshold; in particular, we considered the large aqueous content of the vacuole and selected the threshold very close to the water RI value (e.g., 1.360 has been employed for the reported experiments).
- Up-sampling step in Scheme 1 – Due to the limited imaging spatial resolution of the PCT-FC setup used for experiments, the reconstructed tomograms in Figure 1 and Figure S2a, (Supporting Information) are made of $100 \times 100 \times 100$ voxels. To enhance the resolution, the tomogram in Figure S2a (Supporting Information) is brought to $200 \times 200 \times 200$ voxels by means of linear interpolation. In this way, the imaging spatial resolution is numerically doubled, which means that the CSSI lower bound is intrinsically halved.
- Identification of reference ϵ -cube in Scheme 1 – The previous step of threshold-based coarse segmentation allows identifying a starting reference set that belongs to the organelle to be identified. After dividing the doubled tomogram into non-overlapping cubes having sides measuring ϵ pixels, the central ϵ -cube of the intra-vacuolar volume is chosen as the reference set, as displayed in violet in Figure S2b (Supporting Information). Here, to segment smaller organelles, $\epsilon = 8$ pixels is fixed instead of the $\epsilon = 10$ value used for the nucleus segmentation.^[31] In fact, in reference^[31] we have demonstrated that the ϵ value cannot go under 8 pixels otherwise the CSSI method cannot be implemented regardless of the imaging spatial resolution.



Scheme 1. Generalized CSSI: processing pipeline.

- Rough clustering by WMW test in Scheme 1 – All the other ϵ -cubes (namely, test sets) are iteratively compared to the reference set by means of a statistical hypothesis test –, e.g., the non-parametric Wilcoxon-Mann-Whitney (WMW) test^[30] to decide whether they belong or not to the same organelle (i.e., to the same RI statistical distribution); thus, the rough clustering shown in Figure S2c (Supporting Information) (blue cubes) is obtained.
- Refinement of the organelle cluster in Scheme 1 – The cluster is refined by repeating the statistical comparisons after increasing the spatial resolution of the statistical search, i.e., after dividing the tomogram into $\epsilon/2$ -cubes (Figure S2d, Supporting Information);
- Closing and smoothing operations: PCH in Scheme 1 – The refined cluster is closed by means of a polygonal convex hull (PCH) and then smoothed by Matlab® conventional morphological operators, see Figure S2e (Supporting Information);
- Max-voting in Scheme 1 – The steps in the dashed box in Scheme 1 are repeated $N = 20$ times in order to consider the intrinsic statistical variability of the process, thus obtaining N

PCHs slightly different from each other, which are finally combined through a max-voting strategy in order to obtain the vacuolar organelle convex hull (OCH), see Figure S2f (Supporting Information).

- Down-sampling in Scheme 1 – The $200 \times 200 \times 200$ tomogram with the segmented vacuolar OCH is brought back to its $100 \times 100 \times 100$ starting spatial resolution by means of a down-sampling operation (Figure S3a, Supporting Information).
- Statistical RI thresholding in Scheme 1 – As displayed by the central slice in Figure S3b (Supporting Information), the vacuolar OCH (black dashed line) does not overlap with the expected vacuolar core. Hence, an additional step with respect to the original CSSI is further required. In particular, the voxels belonging to the vacuolar OCH estimated by CSSI correspond to the most representative voxels of the RI statistical distribution about the vacuole. From this statistical distribution, a RI threshold is automatically computed, i.e., the vacuolar volume is obtained as the group of voxels having RI values lower than a RI threshold fixed as the 0.99-quantile of the RI statistical distribution about the vacuolar OCH. The isolevels representation of the isolated vacuolar volume is shown in Figure

S3c (Supporting Information), while the corresponding central slice is reported in Figure S3d (Supporting Information). Remarkably, the dashed black line in Figure S3d (Supporting Information) is now accurately overlapped with the searched vacuole. More precisely, it can be inferred that the vacuolar volume obtained through the CSSI method corresponds to the inner core of the vacuole, i.e., the darkest blue region containing RI voxels with aqueous content, since the statistical inference has been evaluated with respect to the reference set chosen as the central part of the vacuole.

- Identification of peri-vacuolar membrane region in Scheme 1 – In Figure S3d (Supporting Information), outside the segmented vacuolar volume, a ring (light blue region) made of slightly higher RI values is visible. Referring to the structure of the vacuole, it is reasonable to expect that this ring region contains the vacuolar membrane. Notably, the membrane vacuole contains many integral protein complexes, including the proton pumping V-ATPase, several transporters for amino acids and metals, ion channels, or the membrane-associated fusion and fission machinery necessary for vacuole morphology control.^[34] Therefore, the vacuolar membrane is a crowded area that can reasonably support a higher RI than the more aqueous liminal environment or the cytosolic one. Summing up, the vacuolar inner core can be automatically segmented through the generalized CSSI, then the peri-vacuolar membrane region can be recognized as the external shell having the smallest thickness possible with respect to the resolution of the system, as shown in Figure S3e,f (Supporting Information). Here a clarification is due. As the resolution is about 0.5 μm , the external shell is not exactly the vacuolar membrane, which size can be expected to fall into the average size of membrane thickness 4–10 nm.^[36] Although the system resolution is not high enough to localize the membrane accurately, the approach we proposed allowed us to identify the peri-vacuolar area containing it.
- Nucleus identification in Scheme 1 – In the central slice in Figure S3f (Supporting Information), the nucleus is visible at the highest RI values, as it is dense with genetic material. In order to isolate the nucleus of the yeast cells under analysis, the CSSI algorithm cannot be applied even by numerically increasing the imaging spatial resolution. Indeed, the typical size of the nucleus in a yeast cell far exceeds the CSSI lower bound. Nevertheless, the previous identification of the vacuole by generalized CSSI brings as an indirect consequence the possibility to automatically segment the nucleus as well, since a spatial constraint can be fixed by excluding the intracellular volume occupied by the segmented vacuole. In fact, an RI threshold can be automatically fixed such that the voxels with higher RI values are not contained inside the segmented vacuole (i.e., both the inner core and the external shell). The nuclear volume obtained is shown in red in Figure S3g,h (Supporting Information).

In addition, by knowing the 3D space occupied by the vacuole and the nucleus, the nucleus-vacuole junctions (NVJs) can be isolated by means of morphological operations (see the violet volume in Figure S3g,h, Supporting Information). NVJs belong to the membrane contact sites (MCSs), the area of closed apposition between membranes of two organelles.^[37] In eukaryotes,

every organelle establishes MCSs each other for inter-organelle communication thanks to a rapid exchange of small molecules, including ions and lipids.^[38] Particularly, NVJs play a pivotal role in different cellular processes, such as in lipid and ion transport, in lipid droplet biogenesis under stress conditions, and in coordinating a specific type of selective autophagy termed piecemeal microautophagy of the nucleus (PMN).^[39,40] In yeast, NVJs are formed by specialized protein complexes that are locally redistributed to define a flat active zone between the two principal anabolic and catabolic cellular organelles, thereby being in a key position to adapt inter-organelle communication to metabolic demands.^[41,42] Accordingly, it has been shown that glucose deprivation triggers the formation and expansion of NVJs. Moreover, we analyzed yeast cells resuspended in water, which replaces the glucose deprivation conditions favoring the NVJs formation and visualization as an extended and flat area between the two organelles.

In summary, the vacuolar inner core is obtained first; then, the peri-vacuolar membrane region the nucleus, and the vacuole-nucleus contact site can be automatically recognized as an indirect consequence of the application of CSSI to the vacuolar region. Finally, the cytoplasmic region can be considered as the remaining cell volume (Movie S1, Supporting Information).

2.2. Quantitative Specific PCT Analysis of Flowing Yeast Cells

The label-free identification of sub-compartments in the flowing yeast cells is shown in **Figure 2** and Movies S1–S3 (Supporting Information). In particular, Figure 2a,e,i,b,f,j respectively show isolevels representations and the tomographic central slices for the yeast cells undergoing the G1 phase, the late G1 phase, and the S phase (i.e., the same cells shown in Figure 1). In Figure 2, the estimated vacuolar inner core, peri-vacuolar membrane region, and nucleus are simultaneously highlighted. Here, two morphological considerations can be made thanks to the PCT-FC property of reconstructing suspended cells in 3D. The volume growth experienced by the vacuole after the treatment of the yeast cell in water, and the vacuole-nucleus attraction at the contact site (discussed above), leads to a flattening of the nucleus in correspondence to the contact region. Moreover, while in cells at the G1 phase and the late G1 phase (Figure 2a,b,e,f, respectively) nucleus has mainly a roundish 3D shape, and a non-roundish shape can be observed at the S phase in Figure 2i,j. This result is coherent with the duplication of the genetic material that occurs during this cell cycle's phase and that will lead to the detachment of a second nucleus for the daughter cell. In addition to the sole morphological analysis that can be provided by a standard FIFC system, PCT-FC allows also measuring biophysical features related to the segmented intracellular organelles based on their RI values.^[43] For this reason, in Figure 2c,g,k we report the RI histograms corresponding to the 3D RI tomograms in Figure 2a,b,e,f, i,j, respectively. In the retrieved histograms, we highlighted the contributions of the segmented organelles, i.e., the vacuolar inner core, the vacuolar membrane, the nucleus, and the cytoplasmic region. In other words, the generalized CSSI enabled us to move from the analysis of the overall cell histogram (dashed yellow line in Figure 2c,g,k) to its fragmentation into its

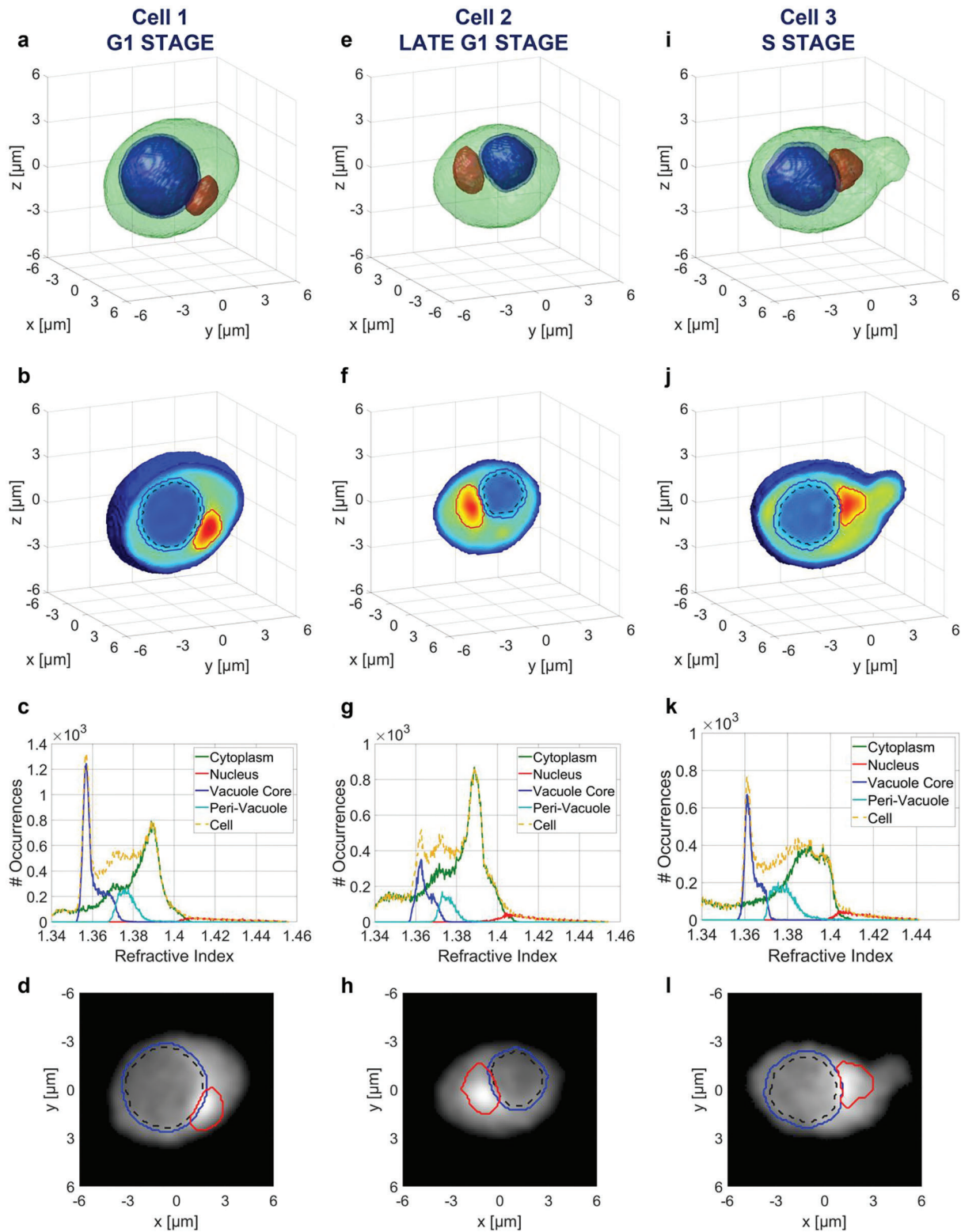


Figure 2. Multi-specificity in budding yeast cells at the a–d) G1 stage (Movie S1, Supporting Information), e–h) late G1 stage (Movie S2, Supporting Information), and i–l) S stage (Movie S3, Supporting Information). a, e, i) Isolevels representation of the PCT-FC tomogram of the yeast cell (green) with highlighted the vacuolar inner core (dark blue), the vacuolar membrane (light blue), and the nucleus (red). b, f, j) Central slice of the PCT-FC tomogram of the yeast cell with highlighted the vacuolar inner core (dashed black line), the vacuolar membrane (solid blue line), and the nucleus (solid red line). c, g, k) RI histograms of both the overall yeast cell (yellow dashed line) and the segmented compartments. d, h, l) QPM obtained after overlaying the contours of the segmented vacuolar inner core (dashed black line), the vacuolar membrane (solid blue line), and the nucleus (solid red line).

components associated with each organelle considered in this work (solid green, red, blue, and light blue lines in Figure 2c,g,k).

Finally, in Figure 2d,h,l we report again the QPMs shown in Figure 1a,d,g, respectively, where we overlaid the contours of the regions corresponding to the vacuolar inner core (dashed black line), the vacuolar membrane (solid blue line), and the nucleus (solid red line) after segmentation. As it occurs for the RI values in the tomographic central slices in Figure 2b,f,j, and also in the QPMs of Figure 2d,h,l, the segmented regions are compatible with the variations in terms of phase values.

In order to validate the proposed vacuole identification method against ground truth, we acquired light microscopy images of the yeast cells in H₂O before inserting them into the PCT-FC system (see Figure 3a). As a quantitative parameter to compare the measurements while compensating any bias due to the different measurements' conditions (PCT-FC works in suspension, light microscopy images are acquired with cells at rest on a Petri dish), we measured the cell-vacuole size scaling, i.e., the ratio between the cell diameter and the diameter of the main roundish vacuole.^[44] We compared the measurements from the 33 cells reconstructed by PCT-FC at the G1 phase to the light microscopy measurements over 100 yeast cells at the same stage and in the same buffer. Results are reported in the boxplot of Figure 3b and show an excellent agreement between the two measurements. Besides, we randomly extracted 1000 subgroups of 33 cells from the 100 ground-truth cells and, for each of them, we computed the *p*-value with the 33 PCT-FC cells related to the cell-vacuole size scaling. At this aim, we have employed the two-sample *t*-student test, thus obtaining a *p*-value of 0.54 ± 0.21 , which suggests that the PCT-FC measurements are in very good agreement with the measurements obtained through the ground-truth technique.

Figure 3c shows the results of further comparison with fluorescence-labeled vacuoles imaged using a confocal microscope (Thunder Imager 3D cell culture microscope). We used the lipid fluorescent probe FM4-64 to decorate the vacuolar membrane of 100 yeast cells. FM4-64 is an amphipathic fluorescent molecule that is partially inserted into the membrane bilayer without passing it. As such, this probe reaches the vacuolar compartment by endocytosis and decorates the limiting vacuolar membrane but not its lumen. Next, we considered the three main diameters of the 3D reconstructed vacuoles. In Figure 3c, we show the boxplots of the vacuolar size, defined as the average size of the three measured diameters, for both the CSSI and the confocal FM. Results are in good agreement with a residual difference between the median values of 0.4 μm. This is explainable and coherent with the expectations since the CSSI-based method distinguishes the lower RI of the vacuole lumen and, for the resolution limit, is less accurate for the peripheral luminal area close to the vacuolar membrane, thereby slightly underestimating the vacuolar size. On the other hand, the fluorescent-based method allows the determination of the vacuolar size by looking at the diffuse fluorescent signal generated by the membrane-bound probe which, by definition, decorates the most peripheral vacuolar layer. Moreover, due to the light diffusion effect, the fluorescent-based method can overestimate the vacuolar size. This is an intrinsic limitation that affects any fluorescence-based microscope and is a further argument for investigating new label-free methods.

As a further testbed, we introduced specificity also in the challenging case of a yeast cell at the G2/M phase, in which the big-

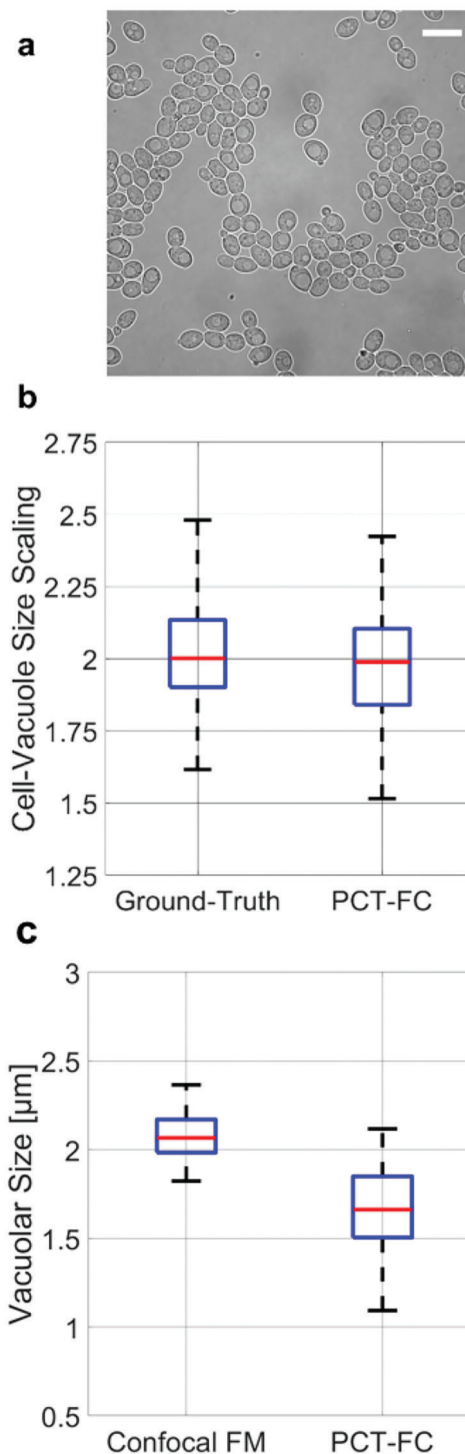


Figure 3. Validation of vacuole segmentation in PCT-FC. a) Example of light microscopy images acquired to measure the ground-truth sizes of cells and their vacuoles. Scale bar: 21.8 μm. b) Box-plot of the cell-vacuole size scaling calculated by the generalized CSSI algorithm in PCT-FC mode (33 cells) compared to the corresponding one related to the ground-truth measurements (100 cells). c) Boxplot of the vacuolar size calculated from the PCT-FC measures and the measures of a confocal FM. The red lines in the boxplots indicate the median values, while the bottom and top blue edges indicate the 25th and 75th percentiles, respectively.

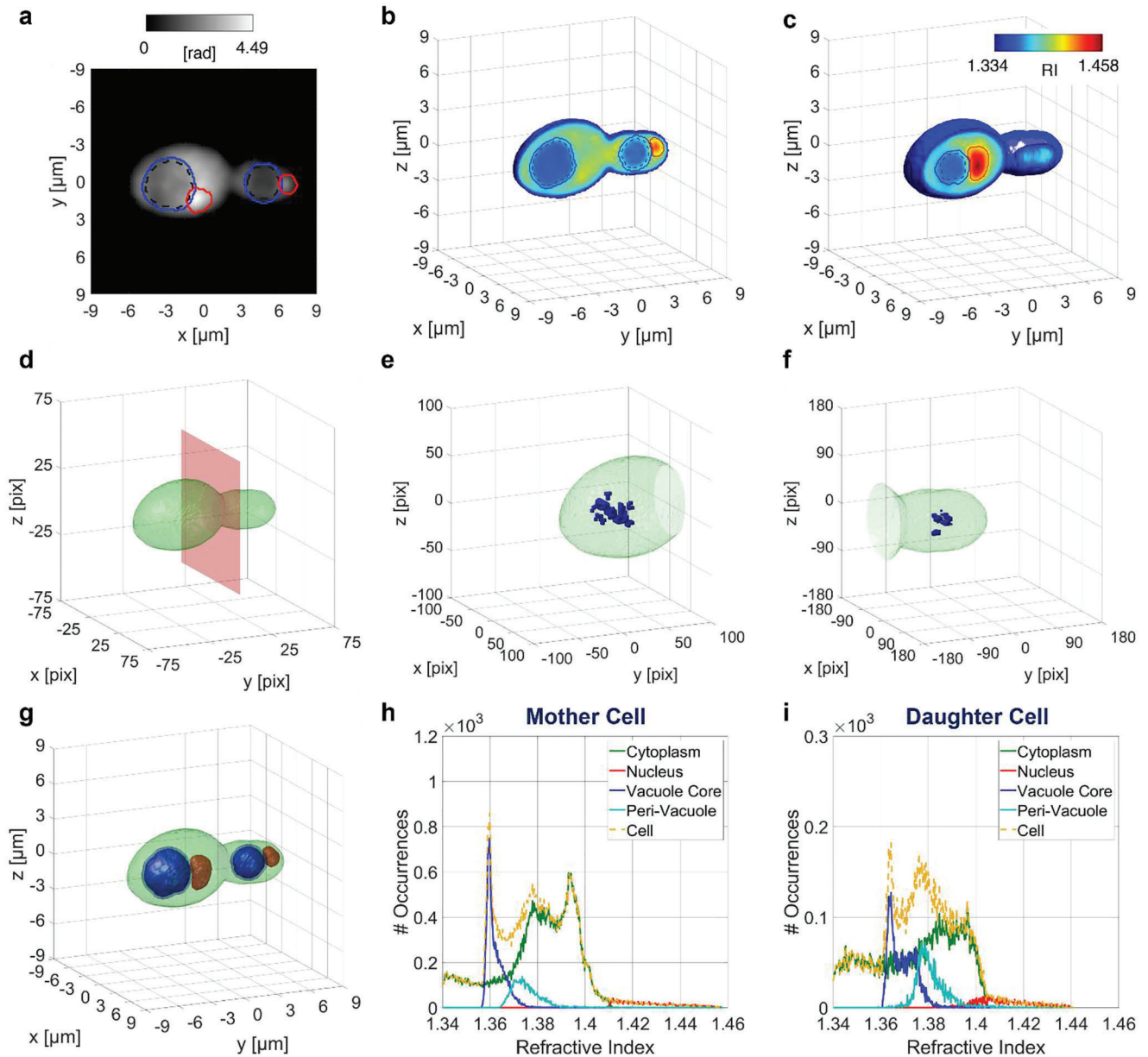


Figure 4. Specificity in a budding yeast cell at the G2/M stage (Movies S4–S6, Supporting Information). a) a QPM taken from the overall sequence used to reconstruct the 3D RI tomogram, with highlighted the vacuolar inner cores (dashed black lines), the vacuolar membranes (solid blue lines), and the nuclei (solid red lines). b,c) Two central slices of the PCT-FC tomogram and a QPM of the yeast cell with highlighted segmented compartments. d) 3D external shape of the yeast cell, with highlighted in red the plane used to divide the mother cell from the daughter cell. e,f) Refined clustering of the $\epsilon/2$ -cubes for the vacuolar segmentation in the mother array (after doubling) and the daughter array (after quadrupling), respectively. g) Isolevels representation of the PCT-FC tomogram of the yeast cell (green) with highlighted the vacuolar inner core (dark blue), the vacuolar membrane (light blue), and the nucleus (red). h,i) RI histograms of both the overall yeast cell (yellow dashed line) and the sole segmented organelles inside the mother cell and the daughter cell, respectively.

ger mother cell and the smaller daughter cell are still attached to each other, even if parts of the vacuole and the nucleus have already migrated from the mother cell to the daughter cell (Movies S4–S6, Supporting Information). This can be clearly seen in a 2D QPM of the recorded sequence in **Figure 4a**, and better observed in two central slices of the corresponding 3D RI tomogram in **Figure 4b,c**. To segment the intracellular organelles, the $190 \times 190 \times 190$ tomographic array is divided into two 3D ar-

rays, i.e., the $100 \times 100 \times 100$ left array containing the mother cell and the $90 \times 90 \times 90$ right array containing the daughter cell (see **Figure 4d**). The generalized CSSI pipeline is applied separately to the two arrays. At this aim, as shown in **Figure 4e**, the array corresponding to the mother cell is numerically doubled up to $200 \times 200 \times 200$ voxels, while the array corresponding to the daughter cell is numerically quadrupled up to $360 \times 360 \times 360$ voxels to consider the smaller vacuolar size (**Figure 4f**). After

identifying the two vacuolar inner cores, the corresponding peri-vacuolar membrane regions and nuclei are identified. Hence, as shown in Figure 4g, we segmented multiple organelles simultaneously in both the mother and daughter cells in the case of a budding yeast cell right before its duplication (see Movies S4–S6, Supporting Information, reporting all the stages of the proposed segmentation pipeline). The boundaries of the segmented compartments are highlighted in Figure 4a–c. The specific RI histograms of the mother cell and the daughter cell are respectively reported in Figure 4h,i. After identifying the organelles and sub-compartments inside the yeast cells, PCT-FC allows measuring, for each of them, quantitative features related to their 3D morphology, 3D location inside living suspended cells, and RI-based parameters. These quantitative measurements are reported in Tables S1–S5 (Supporting Information) about the overall cell, the nucleus and the vacuole-nucleus contact site, the vacuolar core, the peri-vacuolar membrane region, and the cytoplasmic region, respectively, separately for each cell herein shown. In particular, the equivalent radius is the radius of a sphere having the same volume as the analyzed object. The sphericity is the ratio between the surface area of a sphere having the same volume as the analyzed object and the surface area of the object (it is 100% in the case of a perfect sphere). The principal axes' lengths are the lengths of the major axes of the ellipsoid having the same normalized second central moments as the analyzed object. The organelle-cell distance is the distance between the organelle centroid and the cell centroid. The organelle-cell normalized distance is the organelle-cell distance normalized to the cell equivalent diameter. Finally, the dry mass is the amount of non-aqueous content contained inside the analyzed object, i.e.

$$\text{dry mass} = \frac{(\bar{n} - n_0) V}{\alpha} \quad (1)$$

where \bar{n} is the average RI, n_0 is the RI of the surrounding medium, considered homogeneous ($n_0 = 1.334$), V is the object volume, and α is the refractive increment.^[4] The dry mass is one of the most representative parameters accessed by QPI techniques. For example, it has been exploited to classify the cell cycle stage.^[45] When different objects must be compared in terms of dry mass, it is preferable to normalize the dry mass to the object's volume, thus obtaining the dry mass density, which is reported in Tables S1–S5 (Supporting Information). In this way, we observe that the vacuolar cores have a dry mass density around $0.15 \text{ pg } \mu\text{m}^{-3}$, i.e., about 70% of the overall cell dry mass density, while the nuclei have a dry mass density around $0.42 \text{ pg } \mu\text{m}^{-3}$, i.e., twice the overall cell dry mass density. This large difference (the nucleus has almost three times larger dry mass density than the vacuole) is due to the biochemical composition of these two organelles. In fact, nucleus is a dense organelle full of genetic material, while the vacuole is mainly made of water content. Similarly, we observe that the dry mass density measured for the peri-vacuolar membrane is significantly larger than the same parameter measured for the vacuolar core. This result is coherent with the above-mentioned biophysical considerations about the composition of this sub-compartment. It is interesting to note that the vacuole-nucleus contact site exhibits higher dry mass density with respect to both the vacuolar inner core and the cytoplasm. Besides, this parameter measured at the contact site is higher

than the dry mass density measured over the whole peri-vacuolar membrane region. These results are in very good agreement with the expected function of this sub-compartment, discussed above. Indeed, the NVJ is a crowded area, due to the presence of three membranes (i.e., two of them belonging to the nuclear envelope and one to the vacuolar membrane), with a high concentration of specialized protein complexes which structurally and functionally define this compartment, fully supporting the presence of higher RI and dry mass density values.

2.3. Inspection of Segmented Tomograms by Virtual Reality

Intracellular multi-specificity in 3D RI tomograms comes with a problem to tackle, related to the complexity of handling the associated information content. Conventional slice-by-slice representations of the tomograms are not the most suitable way to flexibly inspect the RI distributions associated with the sub-compartments. On the other hand, specificity allows one to move from a quasi-continuous distribution of RIs to statistically accurate isolevel representations of each organelle. Hence, here we investigate a novel modality of fruition of the 3D tomographic flow cytometer outcomes, based on a virtual reality (VR) setting.^[46–49] We show how using a VR kit, it is possible to interact with objects, obtain quantitative information about each sub-compartment, observe them from outside or inside the cell, and visually verify their structure from the preferred perspective in an immersive way.

The immersive and interactive VR tool lends itself well to improving the perception and acquisition of information. Some works like^[46] introduce VR for the first time as an instrument through which the 2D views of a microscope can be transformed into 3D views that can be manipulated interactively. In,^[47] the authors present a VR-based interaction framework in which users can manipulate helical chains of methane in a nanotube, and estimate the user performance during task execution. The work described in^[48] is an example of delivering a more effective and cognitively comprehensible histopathology laboratory than traditional labs. The paper in^[49] highlights how VR increasingly establishes itself as a new technique for visualizing, interacting, and using 3D images in the cellular field. Here we give users the possibility to request on demand the quantitative parameters of the single cell as a whole and, specifically, of each organelle/sub-compartment. Moreover, VR can be used in this framework to enter and travel inside the tomogram, to inspect from the most favorable perspective important sections like, e.g. the organelles' contact and proximity regions. Details on the VR module are provided in the Experimental Section. Since the print medium is not the best way to showcase interactivity, this paragraph proposes a walkthrough of the inspected cells to show the potentialities of the VR application created. An example of the experience tried by a user wearing the VR helmet is shown in Movie S7 (Supporting Information).

There are a few ways in which an immersive environment can enhance the visualization and analysis tasks. In this work, the objective is to provide a better way to inspect 3D data by “scaling” the cells so that a user can roam freely around and inside them. The possibility of showing quantitative analysis more contextually is explored too. After putting on the VR helmet, the user

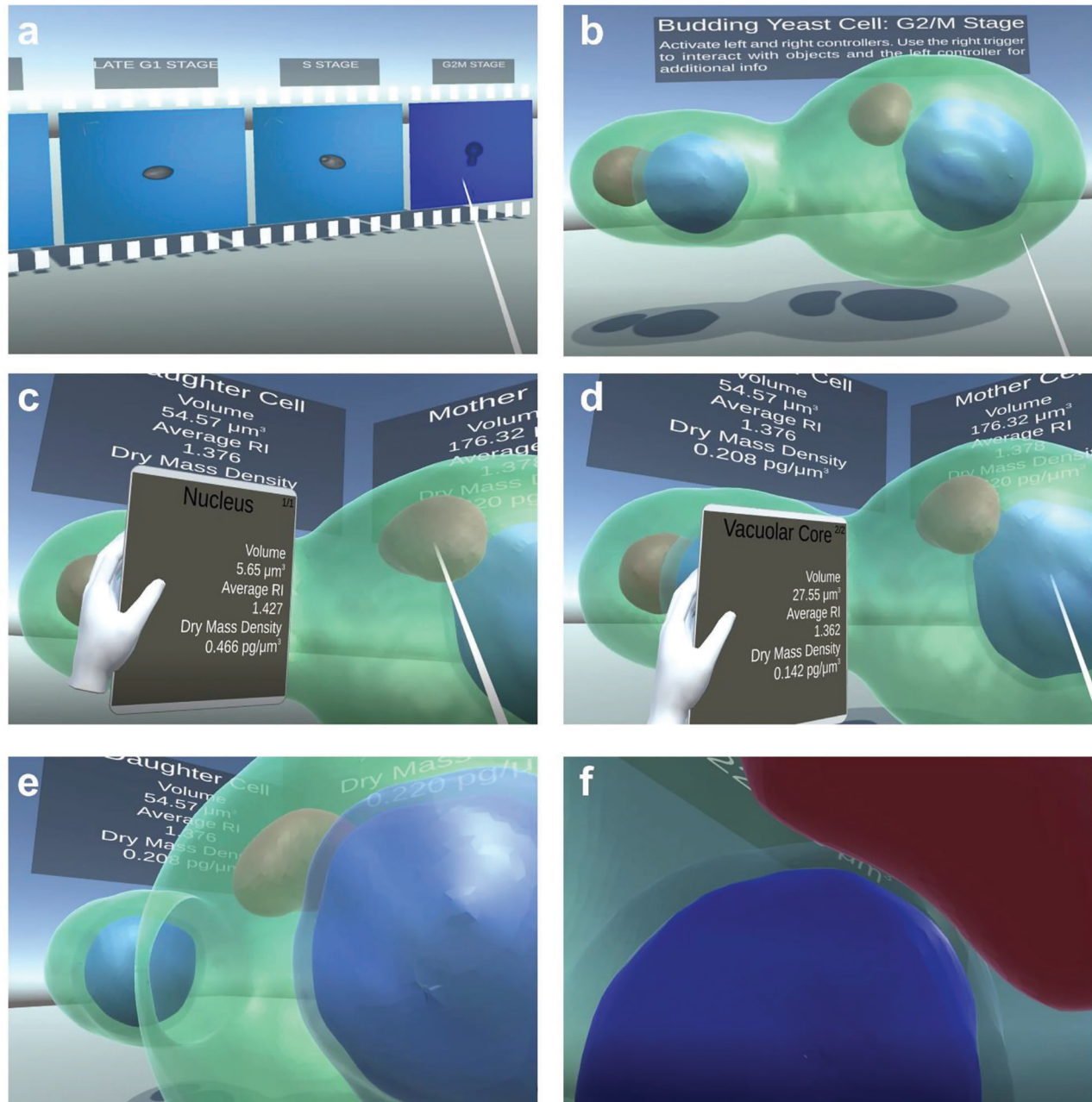


Figure 5. Virtual Reality environment. a) The user wearing the helmet selects the folder with the cells of interest. b) Budding Yeast Cell (G2/M phase) is selected. c) Quantitative biophysical parameters of the mother and daughter cells are displayed. The parameters of the nucleus of the mother cell are retrieved on demand when the user clicks on it with the pointer. d) Vacuolar core parameters are accessed on demand using the pointer. e) The cell can be explored from inside or outside and the inheritance region is shown. f) The user enters inside the cell and can explore the proximity region between the cytoplasmic vacuole and the nucleus from the chosen perspective.

can select the cells to inspect, grouped based on the evolutionary stages. When the user clicks with the pointer on a specific folder, she/he finds himself immersed in an environment where the selected cell can be accessed and analyzed in detail. Selection happens akin to pointing things with a laser pointer. Reporting info back to the user is performed via a tablet present in the virtual environment. Since there is a possibility that the laser pointer ray intersects and might select more than one ob-

ject/organelle, it is possible to switch the organelle of interest with the main trigger of the left controller. The full sequence reported in Movie S7 (Supporting Information) is hereafter described, and summarized in **Figure 5**. After selecting the folder with the cell and the stage of interest (Figure 5a), the user sees the cell in front of him. On the top of the cell the label “Budding Yeast Cell: G2/M Stage” indicates the selected element and the corresponding stage (Figure 5b). After a few seconds, two

tables appear, showing the measured biophysical parameters for the mother and the daughter cells in the budding yeast. In this way, the user can analyze the cell and its organelles from outside. In the next step, the user clicks on the nucleus with the pointer, and a table appears on the tablet, showing the retrieved specific biophysical parameters of this organelle, e.g. volume, dry mass density, and average RI in this case (Figure 5c). In a subsequent step, the user faces the vacuole and its membrane, and by clicking on it, associated tables are shown on the virtual tablet (e.g., the vacuolar core parameters are retrieved, Figure 5d). After these tasks, the user observes the inheritance structure (Figure 5e), then she/he crosses the membrane and looks at the organelles from inside the mother cell. The user continues towards the inheritance structure between the two cells and is able to look at the proximity region between the vacuole and nucleus (the vacuole-nucleus contact site shown in Figure S3g (Supporting Information) is not reported in this example for the sake of simplicity), Figure 5f. At the end, the user leaves the scene and can inspect any of the other cells on demand by using the pointer. The VR application we presented is the first attempt to inspect 3D PCT data in a 3D interactive environment and we believe it has a non-negligible unexplored potential. The VR tool simultaneously allows a 3D fruition of the data and a visual sharing of information with an indefinite number of users. In the future, bringing PCT to the metaverse could bridge the gap between the research community of microscopists, physicians called to judge cells for medical diagnostics, and the general public for entertainment and educational/training use.

3. Conclusion and Discussion

Lack of intracellular specificity is the main limitation factor for all QPI methods. In-flow PCT allows gathering very informative data content at the single cell level in flow cytometry mode. However, a 3D tomogram returns a dense distribution of RIs with sensitivity depending on the optical and cell rotation features, i.e., the number and the range of probing angles. Associating voxels of the tomogram to a certain substructure/organelle is the main pathway to emulate the specificity of FM. In the case of cells spread out on a surface, RI thresholding was used to identify elements with high RI contrast, such as lipid droplets (LDs),^[18] nucleoli,^[19] or monosodium urate crystals,^[20] as well as exogenous gold nanoparticles,^[21] which have high RIs. In the case of a PCT-FC system, we have demonstrated that LDs can be visualized and quantified in 3D suspended/flowing cells by means of an RI threshold.^[22]

As discussed before, AI-based approaches are viable to emulate specificity in 2D QPI and 3D RI tomograms in static or quasi-static conditions.^[24–30] Accurate localization of the 3D fluorescence signal is hard to achieve though. In general, AI-based models that use the 3D fluorescence channel as a ground truth are intrinsically limited in reconstruction accuracy since a network cannot perform better than the reference data it has been trained with. In order to solve the specificity issue in PCT-FC, CSSI has been proposed to identify the voxels belonging to the cell nucleus.^[31] CSSI does not rely on AI and fluorescence examples/ground-truth, but rather it infers the property of a voxel to belong or not to a certain region by means of local statistical tests on the basis of the cell's RI distribution. In this work,

we have generalized the CSSI algorithm (Scheme 1) to obtain specificity on cytoplasmic vacuoles, whose identification in high-throughput flow cytometry mode could have important applications in diagnostics and medicine.^[50–64] Besides the vacuoles and the nuclei, the generalized CSSI strategy reported here is capable of identifying, segmenting, and quantitatively analyzing other cell sub-compartments, i.e., the peri-vacuolar membrane shell, the vacuole-nucleus contact site, the cytoplasmic region (see Figures 2 and 4; Figure S3g, and Tables S1–S5, Supporting Information). We benchmarked the algorithm by tuning the size of vacuoles in yeast cells in different phases of their life cycle. The measure of the cytoplasmic vacuole is in very good agreement with light microscopy observation of yeast cells at the same stage under similar osmotic conditions. The dry mass density measured by PCT-FC is coherent with the biophysical properties of the segmented organelles and compartments, which is a further validation of the effectiveness of the statistical segmentation approach. As a more challenging result, we identified the same organelles/sub-compartments in both the mother and daughter cells belonging to yeast cells subject to the budding process. Four technical challenges have been met in this work:

- i. We handled the case of an organelle that does not necessarily contain the cell central voxel (which was the main starting hypothesis of CSSI). Rather, we used prior biophysical information on the label-free organelle to be isolated.
- ii. We demonstrated the applicability of the CSSI to the vacuoles, i.e., organelles with low RI values and distribution completely different from the RI values of the nucleus.
- iii. Organelles with size challenging the resolution of the optical system have been segmented from tomograms obtained using the rapid FBP reconstruction algorithm rather than the LT one. In our previous work,^[31] the LT algorithm allowed us to improve resolution and RI sensitivity in the tomogram reconstruction, at the cost of computational time. Unlocking the use of the FBP algorithm coupled with the CSSI allows gaining about two orders of magnitude in terms of computational time, which is an important step forward for high-throughput in PCT-FC analysis.
- iv. As an indirect consequence of the generalized CSSI, sub-compartments other than the nucleus and the vacuoles have been localized. Thus, the whole cell RI histogram can be fragmented into its main components, to measure specific information on each sub-compartment in a flow condition.

PCT was already employed to reconstruct the label-free 3D RI distribution of yeast cells. However, the PCT setups employed so far worked in static conditions and were framed inside the two conventional PCT recording principles.^[5,12] In particular, in a previous work based on a static PCT-SR configuration, vacuoles were segmented inside the 3D RI tomograms of suspended yeast cells by means of RI-based thresholding.^[12] However, due to the intraspecies variability, the same RI threshold cannot work in the same way for all the cells of a certain population. Hence, in a PCT-FC experiment in which hundreds/thousands of cells will be recorded, mere thresholding is not a viable and reliable strategy. The CSSI algorithm comes with the advantage of being fully automatic and self-consistent with the information contained within the analyzed cell, independently from the other ones be-

longing to the same population. In addition, the CSSI takes into account the inherent statistical similarities among voxels of the same organelle, therefore the boundary of the vacuole can be found with high accuracy, unlike a manual/custom setting of the RI threshold. Once most of the voxels have been associated with organelles statistically identified, an automatic threshold, well-tailored to the remaining compartment to be isolated is set automatically. In this work, the generalized CSSI was applied to yeast cells as a model cell line. However, its applicability is expected to be extendable to other cell types. Eukaryotic cells contain different membrane-enclosed organelles whose shape and dimension can reflect the health status of the cell since their morphological alteration is generally linked to a dysfunctional pathological situation.^[50,51] Accordingly, the formation of large cytoplasmic vacuolar structures has been identified in many pathologies, such as lysosomal storage diseases (LSDs),^[52] cancer,^[53–57] and viral infections,^[58–60] including the more recent SARS-CoV-2.^[61] Vacuoles have also been found in the macrophages of patients exposed to Gram-negative bacteria lipopolysaccharide.^[62] In addition, in leukocytes, vacuoles are also reported upon exposure to various chemicals.^[63,64] Indeed, many drugs used for oncologic treatment are weak bases that can be protonated and sequestered within lysosomes, thereby causing their vacuolation^[65] and exerting chemoresistance in cancer cells.^[66] Therefore, cytosolic vacuolation can be exploited for different purposes, including diagnosis. Moreover, the formation of lysosomal vacuoles represents a hallmark for LSDs^[67] and either genetic or drug screenings have been conducted to identify which protein machinery drives this expansion or which drugs can revert or prevent it.^[68] In order to exploit CSSI for high-throughput diagnostics, the overall reconstruction and segmentation process, here implemented on a general-purpose desktop computer, could be in the future parallelized and implemented on multicore workstations working on Graphical Processing Units (GPUs).

Furthermore, the possibility to move from a dense RI distribution to an isolevels representation of the tomograms where organelles are accurately segmented, allowed us for the first time to explore a new modality in the fruition of the tomograms using VR. The processed tomograms are the input to the VR system. We have shown that users can enter inside the tomograms of each single cell and explore different perspectives of each of the isolated organelles while receiving specific quantitative information associated with them on demand. The field opens up for data inspection through interaction with additional senses, e.g. tactile stimuli based on the organelles' dry mass and surface roughness. While here we focused on the fruition of segmented tomograms by VR, we foresee for the future a more important exploitation of the tool that could help the tomogram processing, identification of sub-compartments, cell classification, and sorting. We believe this first attempt could trace the route to a novel way of analyzing and sharing such data in the visually interactive metaverse by researchers, biologists, and physicians, for research scopes and also for training, popular science education, and outreach.

4. Experimental Section

Sample Preparation: Baker yeast, *Saccharomyces cerevisiae*, were cultivated in YPD (yeast extract, peptone, dextrose 2%) agar plates starting from a live fresh yeast cube of 25 g commercially available at the super-

market. Specifically, a small portion of the yeast cube was spread on YPD agar plates and incubated at 30 °C for 24 h up to the appearance of white colonies. A single colony was picked up and transferred into a 4 mL liquid YPD tube, and cells were grown for another incubation time of 24 h at 30 °C. Before running the experiment, the optical density (OD) of the yeast culture was determined by measuring the absorbance at 600 nm with a spectrophotometer. According to this value, cells were diluted in 4 mL of YPD up to 0.5OD and grown at 30 °C for 2 h. After that, cells were collected, and YPD media was replaced with 1 mL of sterile H₂O and incubated for 10 min before starting the PCT-FC experiment.

FM4-64 Staining, Microscopy Acquisition, and Vacuole Diameter Analysis: FM4-64 staining was performed as previously described.^[32,69] Briefly, cells were inoculated into a pre-culture in the stationary phase and grown overnight to the logarithmic phase (OD₆₀₀ nm between 0.2 and 0.8) in agitation at 30 °C. After diluting OD₆₀₀ = 0.2 in 1 mL culture, 10 μM FM4-64 was added from a 10 mM stock in DMSO. Cells were incubated for 1 h in agitation conditions at 30 °C and followed by three washing steps with medium without FM4-64 (2 min, 3000 g). After that, cells were incubated for the subsequent chase of 2 h in a medium without FM4-64 to let the probe reach the vacuolar compartment by the endocytic route. After the chase, cells were exposed to different osmotic conditions (i.e., H₂O for the hypotonic and 400 mM NaCl for the hypertonic conditions), Figure S1b (Supporting Information). The temperature was maintained constant during visualization using an environmental control chamber and an objective heater. A Leica Thunder Imaging System (Leica Microsystems Wetzlar, Germany) equipped with a LEICA DFC9000 GTC camera, lumencor fluorescence LED light source, and 100× oil immersion objective was used to acquire Z-slice images. The determination of vacuole diameters was obtained using the ImageJ Fiji software. These were used to assess quantitatively the possibility of tuning the number and size of cytoplasmic vacuoles by acting on the buffer. Briefly, the nm length of each vacuole diameter has been calculated by measuring the number of pixels contained for each diameter and dividing by the number of pixels contained in the internal scale bar (10 μm) obtained from the Thunder Imaging System. 100 vacuole diameters were analyzed for each experimental condition (mock, H₂O, and NaCl). The analysis assessed the effective tuning of the vacuole sizes as an effect of the external medium osmolarity.

PCT-FC Setup: PCT-FC experiments were performed through the opto-fluidic recording system sketched in Figure 6a.^[22] The optical module was a DH microscope in an off-axis configuration based on a Mach-Zehnder interferometer. A polarizing beam splitter (PBS) splits the original coherent beam (532 nm laser) into an object and a reference beam. The ratio between the two beams' intensities was balanced by two Half-Wave Plates (HWP). The object beam illuminated the cells flowing along the microfluidic channel and then it was collected by a high numerical aperture microscope objective (MO1, NA = 1.3) and sent to a tube lens (TL1). Instead, the reference beam passed through a beam expander, a second microscope objective (MO2), and a second tube lens (TL2). The interference between the resulting object and reference waves were produced inside a Beam Splitter (BS) acting as a combiner. Finally, the obtained digital hologram was recorded by the CMOS camera (5120 × 5120 pixels, 4.5 μm each pixel, 30 fps). An example of a recorded digital hologram is shown in Figure 6b. The fluidic module was made of a microfluidic channel (Microfluidic ChipShop 10000107 – 200 μm × 1000 μm × 58.5 mm) in which a laminar flow was generated by an automatic low-pressure pump at about 50 nl s⁻¹. If cells were not exactly in the center of the channel's cross-section, cells underwent a velocity gradient due to the parabolic velocity profile of the laminar flow, which induced their roto-translation along the microchannel. In particular, as sketched in Figure 6b, cells were recorded along the optical z-axis, flow along the y-axis, and mainly rotated around the x-axis, since the field of view (FOV) was fixed in the center with respect to the x-axis and in the bottom with respect to the z-axis.^[22,31] The FOV measures 640 μm × 640 μm (corresponding to 5120 × 5120 pixels), therefore hundreds of digital holograms were recorded per cell at multiple viewing angles.

PCT-FC Numerical Processing: From each 5120 × 5120 digital hologram of the video sequence recorded by the PCT-FC system, several QPMs were numerically computed containing single flowing cells.^[22] At this aim,

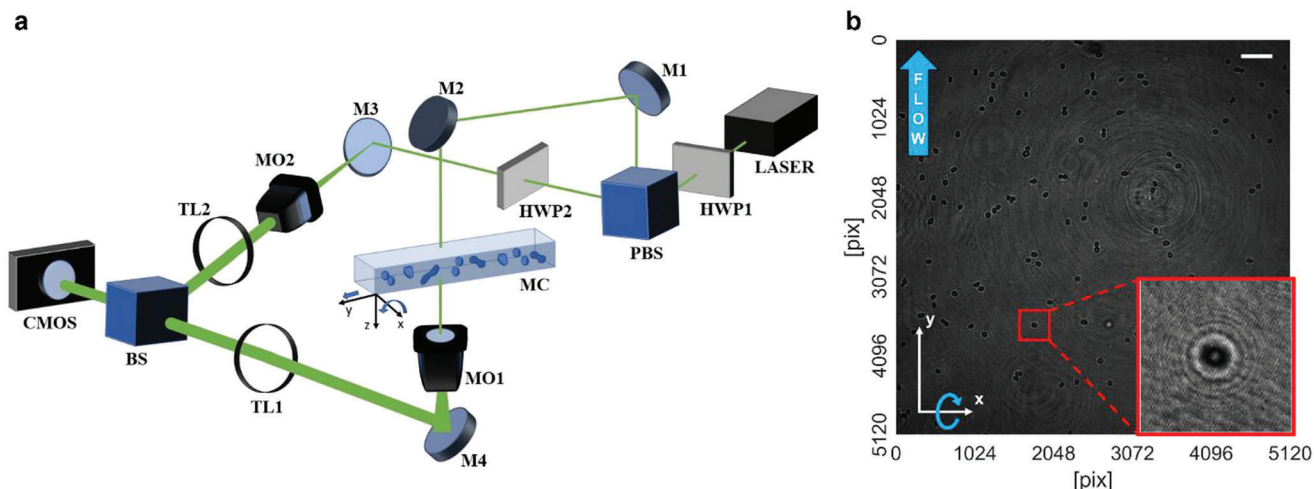


Figure 6. PCT-FC paradigm. a) Opto-fluidic recording system. MO, microscope objective; HWP, half-wave plate; PBS, polarizing beam splitter; M, mirror; TL, tube lens; BS, beam splitter; CMOS, camera. b) Example of a digital hologram recorded by the PCT-FC system, with highlighted in the inset a yeast cell at the G1 phase. The scale bar is 50 μm .

384 \times 384 regions of interest (ROIs) were cropped around the cells. Thanks to the off-axis configuration of the DH microscope, the diffraction orders did not overlap in the Fourier domain, so a Fourier band-pass filtering was employed to select the real diffraction order and demodulate each holographic ROI.^[8] Then, cells were numerically refocused by exploiting the DH features.^[22] In particular, the Angular Spectrum method was implemented to numerically propagate the holographic ROI along the optical axis, and then an image contrast-based metric (i.e., the Tamura Coefficient) was minimized to find the cell's focal distance. After extracting the argument of the refocused complex wavefront, a reference hologram was subtracted to remove residual optical aberrations, the 2D windowed Fourier transform filtering was used to denoise the resulting phase map, and the PUMA algorithm was employed for the phase unwrapping.^[70] The obtained QPMs were centered with respect to their weighted centroids. For each flowing cell, its rolling angles were estimated by exploiting its QPMs, holographic tracking, and microfluidic properties. Finally, for each cell, the FBP algorithm was fed by the QPMs and the corresponding rolling angles to reconstruct its 3D RI tomogram.^[10]

VR Module: The application was built using Unity^[71] as the development platform, while on the hardware side, a workstation with an nVidia Quadro A4500 and HTC VIVE Pro 2^[72] were used. The prototype used OpenXR for interfacing with the VR headset and the associated controllers. The prototype exploited HTC VIVE Pro 2 and its base stations for providing the possibility to freely roam in the proposed environment, while at the same time retaining the possibility to “teleport” to a new location, without physical locomotion, when it was more convenient for the user. For the sake of the graphical representation, tomograms were processed in order to obtain higher-resolution meshes. The smoothing process was beneficial for the representation and for the user interactions as well. Indeed, smoothing each object enabled to obtain a more “organic” feel, where the discretization imposed by the limits of current scanning technologies involved in getting the tomogram voxels almost “vanished” when the user was immersed in the environment. A second polygonal version of each object-organelle was also obtained by “decimating” the higher resolution mesh – this was used for collision detection, internally used by the VR system for understanding which objects the user was pointing to. In addition to the helmet position for exploring the virtual environment from different perspectives, interaction was enabled by the Vive wand left and right controllers, used for selecting organelles with the virtual laser pointer and obtaining contextual information via the virtual tablet. Moreover, aggregate data, for example, related to the mother and daughter cells as a

whole, were shown on camera-facing billboard panels on top of the cells, so that the user could always read them more easily.

Supporting Information

Supporting Information is available from the Wiley Online Library or from the author.

Conflict of Interest

V.B., D.P., L.M., P.M., and P.F. have filed a patent (pending patent PCT/IB2022/056625) about some key aspects described in the article. The other authors declare no competing interests.

Author Contributions

V.B. and M.D.A. contributed equally to this work. P.F., V.B., and M.D.A. conceived the research. L.M. and G.G. designed the microscopy system and performed the PCT-FC measurements. D.P. and P.M. developed PCT algorithms. V.B. and D.P. analyzed the data. M.D.A. and G.S. prepared the cell cultures and performed the light microscopy and confocal measurements. N.M., M.D.S., and E.S. conceptualized the developed VR approach and realized the software suite. V.B., D.P., and M.D.A. wrote the original draft. T.R., P.F., interpreted the results and reviewed the manuscript draft. T.R., E.S., and P.F. supervised the research in each group. All authors discussed the data. All authors contributed and revised the manuscript. All authors had given approval for the final version of the manuscript.

Data Availability Statement

The data that support the findings of this study are available from the corresponding author upon reasonable request.

Keywords

drug delivery, diagnostics, disease prevention, imaging, nanomedicines, pharmacology, therapeutics, theranostics

Received: April 4, 2023
Revised: August 14, 2023
Published online:

- [1] Y. Han, Y. Gu, A. C. Zhang, Y. H. Lo, *Lab Chip* **2016**, *16*, 4639.
- [2] M. Doan, I. Vorobjev, P. Rees, A. Filby, O. Wolkenhauer, A. E. Goldfeld, J. Lieberman, N. Barteneva, A. E. Carpenter, H. Hennig, *Trends Biotechnol.* **2018**, *36*, 649.
- [3] N. S. Barteneva, E. Fasler-Kan, I. A. Vorobjev, *J. Histochem. Cytochem.* **2012**, *60*, 723.
- [4] Y. Park, C. Depeursinge, G. Popescu, *Nat. Photonics* **2018**, *12*, 578.
- [5] J. Lim, W. Liang, A. A. Savchenkov, A. B. Matsko, L. Maleki, C. W. Wong, *Light: Sci. Appl.* **2019**, *8*, 1.
- [6] T. L. Nguyen, S. Pradeep, R. L. Judson-Torres, J. Reed, M. A. Teitell, T. A. Zangle, *ACS Nano* **2022**, *16*, 11516.
- [7] Lu Xin, W. Xiao, L. Che, J. Liu, L. Miccio, V. Bianco, P. Memmolo, P. Ferraro, X. Li, F. Pan, *ACS Omega* **2021**, *6*, 31046.
- [8] M. K. Kim, *SPIE Rev* **2010**, *1*, 018005.
- [9] Ç. Işıl, K. De Haan, Z. Göröcs, H. C. Koydemir, S. Peterman, D. Baum, F. Song, T. Skandakumar, E. Gumustekin, A. Ozcan, *ACS Photon* **2021**, *8*, 1232.
- [10] W. Choi, C. Fang-Yen, K. Badizadegan, S. Oh, N. Lue, R. R. Dasari, M. S. Feld, *Nat. Methods* **2007**, *4*, 717.
- [11] P. Y. Liu, L. K. Chin, W. Ser, H. F. Chen, C.-M. Hsieh, C.-H. Lee, K.-B. Sung, T. C. Ayi, P. H. Yap, B. Liedberg, K. Wang, T. Bourouina, Y. Leprince-Wang, *Lab Chip* **2016**, *16*, 634.
- [12] M. Habaza, B. Gilboa, Y. Roichman, N. T. Shaked, *Opt. Lett.* **2015**, *40*, 1881.
- [13] F. Liang, J. Zhu, H. Chai, Y. Feng, P. Zhao, S. Liu, Y. Yang, L. Lin, L. Cao, W. Wang, *Small Methods* **2023**, *7*, 2201492.
- [14] D. Pirone, D. Sirico, L. Miccio, V. Bianco, M. Mugnano, P. Ferraro, P. Memmolo, *Lab Chip* **2022**, *4*.
- [15] B. Ge, Y. He, M. Deng, M. H. Rahman, Y. Wang, Z. Wu, C. H. N. Wong, M. K. Chan, Y. Ho, L. Duan, Z. Yaqoob, P. T. C. So, G. Barbastathis, R. Zhou, "Single-frame label-free cell tomography at speed of more than 10,000 volumes per second," *arXiv:2202.03627*.
- [16] Y. Sung, N. Lue, B. Hamza, J. Martel, D. Irimia, R. R. Dasari, W. Choi, Z. Yaqoob, P. So, *Phys. Rev. Appl.* **2014**, *1*, 014002.
- [17] A. Kleiber, D. Kraus, T. Henkel, W. Fritzsche, *Lab Chip* **2021**, *21*, 3655.
- [18] S. Park, J. W. Ahn, Y. Jo, H.-Y. Kang, H. J. Kim, Y. Cheon, J. W. Kim, Y. Park, S. Lee, K. Park, *ACS Nano* **2020**, *14*, 1856.
- [19] T.-K. Kim, B.-W. Lee, F. Fujii, J. K. Kim, C.-G. Pack, *Cells* **2019**, *8*, 699.
- [20] S. Park, L. Lee, H. Kim, J. E. Kim, S. Lee, S. Yoon, S. Shin, H. Kang, Y. Park, J. J. Song, S. Lee, *Sci. Rep.* **2021**, *11*, 10019.
- [21] D. Kim, N. Oh, K. Kim, S. Lee, C-Gi Pack, Ji-Ho Park, Y. Park, *Methods* **2018**, *136*, 160.
- [22] D. Pirone, D. Sirico, L. Miccio, V. Bianco, M. Mugnano, D. del Giudice, G. Pasquinelli, S. Valente, S. Lemma, L. Iommarini, I. Kurelac, P. Memmolo, P. Ferraro, *Opto-Electron. Adv.* **2023**, *6*, 220048.
- [23] D. Kim, S. Lee, M. Lee, J. Oh, S. Yang, Y. Park, in *Advanced Imaging and Bio Techniques for Convergence Science*, Springer, Berlin **2021**, 211.
- [24] Y. Rivenson, T. Liu, Z. Wei, Y. Zhang, K. De Haan, A. Ozcan, *Light: Sci. Appl.* **2019**, *8*, 23.
- [25] N. Borhani, A. J. Bower, S. A. Boppart, D. Psaltis, *Biomed. Opt. Express* **2019**, *10*, 1339.
- [26] Y. Rivenson, H. Wang, Z. Wei, K. De Haan, Y. Zhang, Y. Wu, H. Günaydin, J. E. Zuckerman, T. Chong, A. E. Sisk, L. M. Westbrook, W. D. Wallace, A. Ozcan, *Nat. Biomed. Eng.* **2019**, *3*, 466.
- [27] M. E. Kandel, Y. R. He, Y. J. Lee, T. H.-Yu Chen, K. M. Sullivan, O. Aydin, M. T. A. Saif, H. Kong, N. Sobh, G. Popescu, *Nat. Commun.* **2020**, *11*, 6256.
- [28] Y. N. Nygate, M. Levi, S. K. Mirsky, N. A. Turko, M. Rubin, I. Barnea, G. Dardikman-Yoffe, M. Haifler, A. Shalev, N. T. Shaked, *Proc. Natl. Acad. Sci. USA* **2020**, *117*, 9223.
- [29] J. Lee, H. Kim, H. Cho, Y. Jo, Y. Song, D. Ahn, K. Lee, Y. Park, S.-J. Ye, *IEEE Access* **2019**, *7*, 83449.
- [30] Y. Jo, H. Cho, W. S. Park, G. Kim, D. Ryu, Y. S. Kim, M. Lee, S. Park, M. J. Lee, H. Joo, H. Jo, S. Lee, S. Lee, H.-S. Min, W. Do Heo, Y. Park, *Nat. Cell Biol.* **2021**, *23*, 1329.
- [31] D. Pirone, J. Lim, F. Merola, L. Miccio, M. Mugnano, V. Bianco, F. Cimmino, F. Visconte, A. Montella, M. Capasso, A. Iolascon, P. Memmolo, D. Psaltis, P. Ferraro, *Nat. Photonics* **2022**, *16*, 851.
- [32] M. D'agostino, H. J. Risselada, A. Lürick, C. Ungermann, A. Mayer, *Nature* **2017**, *551*, 634.
- [33] A. Aufschnaiter, S. Büttner, *Bioch. Biophys. Acta—Molecul. Cell Res.* **2019**, *1866*, 957.
- [34] E. Wiederhold, T. Gandhi, H. P. Permentier, R. Breitling, B. Poolman, D. J. Slotboom, *Mol. Cell. Proteomics* **2009**, *8*, 380.
- [35] M. B. Mayhew, E. S. Iversen, A. J. Harterink, *J. R. Soc. Interface* **2017**, *14*, 20160993.
- [36] S. Ferretti, S. Bianchi, G. Frangipane, R. Di Leonardo, *Sci. Rep.* **2021**, *11*, 7610.
- [37] L. Scorrano, M. De Matteis, S. Emr, F. Giordano, G. Hajnóczky, B. Kornmann, L. L. Lackner, T. P. Levine, L. Pellegrini, K. Reinisch, R. Rizzuto, T. Simmen, H. Stenmark, C. Ungermann, M. Schuldiner, *Nat. Commun.* **2017**, *10*, 2019.
- [38] W. A. Prinz, A. Toulmay, T. Balla, *Nat. Rev. Mol. Cell Biol.* **2020**, *21*, 7.
- [39] H. Hariri, S. Rogers, R. Ugrankar, Y. L. Liu, J. R. Feathers, W. M. Henne, *EMBO Rep.* **2018**, *19*, 57.
- [40] P. Roberts, S. Moshitch-Moshkovitz, E. Kvam, E. O'Toole, M. Winey, D. S. Goldfarb, *Mol. Biol. Cell* **2003**, *14*, 129.
- [41] S. T. Castano, C. Peselj, V. Kohler, L. Habernig, L. Berglund, M. Ebrahimi, F. Vögtle, J. Höög, C. Andréasson, S. Büttner, *Cell Rep.* **2021**, *34*, 1.
- [42] J. Frallicciardi, J. Melcr, P. Signou, S. J. Marrink, B. Poolman, *Nat. Commun.* **2021**, *12*, 2022.
- [43] D. Jin, R. Zhou, Z. Yaqoob, P. T. So, *J. Opt. Soc. Am. B* **2017**, *34*, B64.
- [44] Y.-H. M. Chan, W. F. Marshall, *Biophys. J.* **2014**, *106*, 1986.
- [45] Y. R. He, S. He, M. E. Kandel, Y. J. Lee, C. Hu, N. Sobh, M. A. Anastasio, G. Popescu, *ACS Photonics* **2022**, *9*, 1264.
- [46] S. Ferretti, S. Bianchi, G. Frangipane, R. Di Leonardo, *Sci. Rep.* **2021**, *11*, 7610.
- [47] M. O'Connor, H. M. Deeks, E. Dawn, O. Metatla, A. Roudaut, M. Sutton, L. M. Thomas, B. R. Glowacki, R. Sage, P. Tew, M. Wonnacott, P. Bates, A. J. Mulholland, D. R. Glowacki, *Sci. Adv.* **2018**, *4*, aat2731.
- [48] J. Qing, Gu Cheng, X-Qi Ni, Yi Yang, W. Zhang, Z. Li, *Sci. Rep.* **2022**, *12*, 5492.
- [49] A. P. R. Johnston, J. Rae, N. Ariotti, B. Bailey, A. Lilja, R. Webb, C. Ferguson, S. Maher, T. P. Davis, R. I. Webb, J. Mcghee, R. G. Parton, *Traffic* **2017**, *19*, 105.
- [50] J. P. Luzio, P. R. Pryor, N. A. Bright, *Nat. Rev. Mol. Cell Biol.* **2007**, *8*, 622.
- [51] M. E. G. Araujo, G. Liebscher, M. W. Hess, L. A. Huber, *Traffic* **2020**, *21*, 60.
- [52] A. R. A. Marques, P. Saftig, *J. Cell Sci.* **2019**, *132*, jcs221739.
- [53] M. R. Ambrosio, P. P. Piccaluga, M. Ponzoni, B. J. Rocca, V. Malagnino, M. Onorati, S. Lazzi, *PLOS ONE* **2012**, *7*, e44315.
- [54] D. T. Lynch, K. Foucar, *Blood, J. Am. Soc. Hemat.* **2016**, *127*, 3292.
- [55] O. Ballo, J. Stratmann, H. Serve, B. Steffen, F. Finkelmeier, C. Brandts, *PLoS One* **2019**, *14*, 0223013.
- [56] J. Song, B. Shang, Y. Pei, M. Shi, X. Niu, L. Dou, E. K. Drokow, F. Xu, Y. Bai, K. Sun, *Leukemia Res.* **2021**, *109*, 106638.
- [57] Y. Zhao, E. Wang, *Am. J. Med. Sci.* **2021**, *362*, 27.
- [58] A. V. Shubin, I. V. Demidyuk, N. A. Lunina, A. A. Komissarov, M. P. Roschina, O. G. Leonova, S. V. Kostrov, *BMC Cell Biology* **2015**, *16*, 4.

- [59] R. D. Satria, T.-W. Huang, M.-K. Jhan, T.-J. Shen, Po-C Tseng, Y.-T. Wang, Z.-Yu Yang, C.-H. Hsing, C.-F. Lin, *J. Immunol. Res.* **2021**, 2021, 6654617.
- [60] B. Monel, A. A. Compton, T. Briel, S. Amraoui, J. Burlaud-Gaillard, N. Roy, C. Demangel, E. Simon-Lorière, A. Moris, P. Roingeard, A. Amara, O. Schwartz, *EMBO J.* **2017**, 36, 1653.
- [61] A. Singh, N. Sood, V. Narang, A. Goyal, *BMJ Case Reports CP* **2020**, 13, e236117.
- [62] A. O. Wong, M. Marthi, Z. I. Mendel, B. Gregorka, M. S. Swanson, J. A. Swanson, *Mol. Biol. Cell* **2018**, 29, 657.
- [63] R. J. Davidson, J. L. McPhie, *J. Clin. Pathol.* **1980**, 33, 1193.
- [64] T. Aki, A. Nara, K. Uemura, *Cell Biol. Toxicol.* **2012**, 28, 125.
- [65] X. Zhai, Y. E. Hiani, *Cancers* **2020**, 12, 3669.
- [66] X. Wang, Z. Haiyun, C. Xiaozhuo, *Cancer Drug Res* **2019**, 2, 141.
- [67] E. Roy, J. Bruyère, P. Flamant, S. Bigou, J. Ausseil, S. Vitry, J. M. Heard, *Hum. Mol. Genet.* **2012**, 21, 1481.
- [68] S. F. Garbade, M. Zielonka, K. Mechler, S. Kölker, G. F. Hoffmann, C. Staufner, E. Mengel, M. Ries, *PLoS One* **2020**, 15, e0230898.
- [69] M. D'agostino, H. J. Risselada, A. Mayer, *Embo Report* **2016**, 17, 1590.
- [70] J. M. Bioucas-Dias, G. Valadao, *IEEE Trans. Image Process.* **2007**, 16, 698.
- [71] <https://unity.com/> (accessed: August 2023).
- [72] <https://www.vive.com/us/product/vive-pro2/overview/> (accessed: August 2023).